Estimates of Wind Energy Input to the Ekman Layer in the Southern Ocean from Surface Drifter Data

Shane Elipot

Scripps Institution of Oceanography, University of California, San Diego
present affiliation: The cooperative Institute for Marine and Atmospheric

Studies, 4600 Rickenbacker Causeway, Miami FL 33149

(shane.elipot@noaa.gov)

Sarah T. Gille

Scripps Institution of Oceanography and Department of Mechanical and

Aerospace Engineering, University of California, San Diego

Shane Elipot, Scripps Institution of Oceanography, University of California, San Diego

present affiliation: The cooperative Institute for Marine and Atmospheric Studies, 4600 Ricken-

backer Causeway, Miami FL 33149 (shane.elipot@noaa.gov)

Sarah Gille, Scripps Institution of Oceanography and Department of Mechanical and Aerospace

Engineering, University of California, San Diego LA Jolla, CA, 92093-0230

Abstract.   The energy input to the upper ocean Ekman layer is assessed

for the Southern Ocean by examing the rotary cross-spectrum between wind

stress and surface velocity from frequencies between 0 and 2 cpd. The wind

stress is taken from ECMWF ERA40 reanalysis, and drifter measurements

from 15 m depth are used to represent surface velocities, with an adjustment

to account for the vertical structure of the upper ocean.

The combination of a stronger anticyclonic wind stress forcing associated

with a greater anticyclonic response makes the contribution from the anti-

cyclonic frequencies dominate the wind energy input.

The latitudinal and seasonal variations of the wind energy input to the Ek-

man layer are closely related to the variations of the wind stress, both for

the mean and for the time-varying components. The contribution from the

near-inertial band follows a different trend, increasing from $30°$ S to about

$45°$ S and decreasing further south, possibly a consequence of the lack of vari-

ance in this band in the drifter and wind stress data.

Uncertainties in the analysis may be as large as 30%, but are nonetheless

sufficient to show the relative importance of time-averaged, subinertial, and

near-inertial wind forcing in transfering energy from the atmosphere to the

ocean at the local scale. The high frequency forcing of the ocean is related

to the sources of kinetic energy and near-inertial waves that are in turn re-

lated to the mixing of the ocean and the global overturning circulation.

1. Introduction

1.1. A spectral view of the wind energy input

The transfer of mechanical energy from the atmosphere to the ocean takes place through various physical mechanisms that can be distinguished by the time scales on which they occur. This study makes use of surface drifter data to examine the wind energy input to the Ekman layer on time scales ranging from low-frequency 40-day periods to near near-inertial frequencies.

First, at low frequencies, the wind stress $\boldsymbol{\tau}$ works on the ocean general circulation (represented by the geostrophic velocity $\mathbf{u}_g$ at the surface) as:

$$\boldsymbol{\tau} \cdot \mathbf{u}_g \equiv \mathbf{U}_e \cdot \nabla p_s / \rho. \tag{1}$$

Eq. (1) can be seen as either a direct generation of geostrophic kinetic energy or as an increase in potential energy by the work of the Ekman transport $\mathbf{U}_e$ against the pressure forces at the surface $\nabla p_s / \rho$ [*Gill et al.*, 1974; *Fofonoff*, 1981], with ρ the water density. *Weijer and Gille* [2005] showed that the potential energy framework is more germane to the energetics of a numerical model of the Southern Ocean. *Wunsch* [1998] estimated the left-hand side of Eq. (1) by using altimeter-derived geostrophic velocities and wind stress field analyses for the 1992-96 time period. In his estimate, 95% of wind energy input came from the time mean components of $\boldsymbol{\tau}$ and $\mathbf{u}_g$. Over the global ocean, the maximum energy input rates were greater than 20×10^{-3} W m^{-2} and were found in the Southern Ocean (his Fig. 2). Moreover, 70% of the wind work integrated over the surface of the global ocean was found south of 40° S. *Huang et al.* [2006] studied the decadal variability of this energy input from both altimetry data and numerical model outputs. They found that

the ACC region is where most of the variability is found for the 1979-2003 time period

and furthermore that it is increasingly dominant in the global integral. More recent work

has taken into account the influence of the current on the atmospheric stress [*Duhaut*

and Straub, 2006; *Hughes and Wilson*, 2008]. Using extended observations, *Hughes and*

Wilson [2008] updated Wunsch's estimates, reaching the same general conclusions, albeit

with a decrease in the global integral because of the definite negative contribution to the

wind work due to the effect of oceanic currents on atmospheric wind stress.

Second, at high frequencies, near-inertial motions are triggered in the mixed layer by

rapid, small-scale wind stress fluctuations [e.g. *D'Asaro*, 1985b; *Poulain*, 1990]. Resonance

can occur when the wind stress itself contains a significant rotary spectral component at

the inertial frequency [e.g. *Crawford and Large*, 1996]. The energy flux at near-inertial

frequencies has attracted interest, because it is potentially oriented downward towards

the ocean interior by propagating internal waves [e.g. *D'Asaro et al.*, 1995]. These waves

eventually dissipate and can drive diapycnal mixing [*Gregg*, 1987]. The energy flux to

mixed-layer near-inertial motions has been estimated from wind stress and ocean velocities

measured at mooring locations [*D'Asaro*, 1985a] or more recently from global wind stress

analyses [*Alford*, 2001; *Watanabe and Hibiya*, 2002; *Alford*, 2003]. In these global studies,

the inertial velocities $\mathbf{u}_i$ were inferred from *Pollard and Millard*'s (1970) damped slab-

layer model for which the inertial currents are uniform in the vertical. By using either

numerical integration in time or spectral resolution of the equations, the wind energy input

was computed as $\boldsymbol{\tau} \cdot \mathbf{u}_i$. *Alford* [2003] also considered depth-uniform Ekman velocities $\mathbf{u}_e$

arising from a time-varying Ekman transport, because their energy is also available for

dissipation, but found their impact to be modest. For the period 1989-95, the average

zonal-mean energy input rate at 40° S was about 3×10^{-3} W m^{-2} (his Fig. 1). However,

this value may be too large since *Plueddemann and Farrar* [2006] showed that the slab

layer model systematically results in an overestimation of the work done on mixed-layer

inertial currents, largely because a slab model lacks dissipation on short time scales.

Third, energy fluxes seem to take place at intermediate or "sub-inertial" frequencies

through Ekman dynamics. Vertically-sheared Ekman currents are expected to exist for

all forcing frequencies according to *Gonella* [1972] "extensions" of *Ekman*'s (1905) theory.

He first derived several transfer functions that provide a mathematical representation

of the wind-driven velocity as a function of depth and forcing frequency. *Elipot and*

Gille [2008] studied the theoretical linear transfer functions arising from nine variants of

the Ekman model, which differed in the parameterization of the vertical eddy viscosity

and the boundary condition at the bottom on the wind-driven layer. Although these

transfer functions vary in the details, in general, the predicted Ekman velocities $\mathbf{u}_e$ spiral

with depth from the surface and rotate along with the forcing wind stress vector. The

transfer functions all predict a stronger response when the frequency of the forcing is

anticyclonic (counterclockwise or positive in the Southern Hemisphere) than when it is

cyclonic. They also exhibit either an unbounded or a maximum resonant response at

the inertial frequency. While the Ekman currents themselves should play a role in the

wind energy input into geostrophic currents via Eq. (1), maintaining the Ekman spiral

requires dissipation within the Ekman layer, or a wind energy input rate "to the Ekman

layer". *Elipot and Gille*'s (2008) results showed that the best models to explain drifter

observations in the Southern Ocean have a bounded response at the inertial frequency

at which there is a zero cross-wind component of the wind-driven velocity, and the wind

energy input is therefore maximal.

Wang and Huang [2004] estimated the wind energy input to the Ekman layer by using the transfer function to compute the ocean surface Ekman velocities $\mathbf{u}_e$ from wind stress analyses, assuming that the Ekman model with a constant vertical viscosity and infinite depth ocean applied. They set the Ekman depth to be proportional to the mean friction velocity computed from the wind stress and inversely proportional to the Coriolis parameter. The total wind energy input into the Ekman layer was then obtained by summing the dot product $\boldsymbol{\tau} \cdot \mathbf{u}_e$ over all frequency components. They found that the global integral for this energy input is also dominated by the contribution from the Southern Hemisphere. Examination of Fig. 3 in *Wang and Huang* [2004] reveals that this is mainly due to the strong winds over the Southern Ocean and notably large values over the ACC of about 20×10^{-3} W m^{-2}. They also computed the changes of the global energy input to the Ekman layer over the 1948-2002 time period, which *Huang et al.* [2006] subsequently attributed to wind stress variability in the equatorial region and in the Southern Ocean.

1.2. Does the wind energy input into the Ekman layer matter?

We will show in this paper that the observed co-spectrum between wind stress and oceanic velocities as measured by drifters at 15 m is representative of a momentum flux from the atmosphere to the ocean. This flux takes place at a wide range of frequencies, from low to "sub-inertial" and inertial frequencies. The wind work on the geostrophic circulation is actually a source of mechanical energy for the interior ocean [*Stern*, 1975], but previous studies have not resolved how the wind works on ageostrophic motions, nor have they explained how the generation of ageostrophic motions leads to a transfer of

114 mechanical energy to the ocean interior, well below the surface [*Ferrari and Wunsch*,

115 2008; *Plueddemann and Farrar*, 2006]. Thus one may ask if the third pathway for energy

116 input described above, due to subinertial osciallations, is a relevant source for the energy

117 needed to sustain global meridional overturning circulation.

118 *Von Storch et al.* [2007] derived a mechanical energy budget for output from a high-

119 resolution general circulation model that represented vertical mixing with the nonlocal

120 K profile Parameterization (KPP) of *Large et al.* [1994]. Their analysis showed that the

121 power provided by the wind at the sea surface was not separated between the work done

122 on the geostrophic and ageostrophic circulation, because both components contributed to

123 the total energy transfered down the water column. The dominant terms in the energy

124 equation appear to be the pressure work and the shear-induced stress but the relative

125 importance of these two terms was seen to vary as a function of depth. Overall, their

126 results suggested that about 30% of the total wind energy input, through geostrophic and

127 ageostrophic pathways, is passed through the interior ocean, while the remaining 70%

128 is dissipated locally or converted to potential energy in the upper ocean. These results

129 suggested that it is therefore necessary to estimate all pathways of wind energy input at

130 the surface of the ocean.

131 *Von Storch et al.* [2007] did not distinguish the inertial band contribution from the

132 the contribution due to Ekman dynamics at other frequencies. This is understandable,

133 because the concept of a slab layer at near-inertial frequencies is incompatible with the

134 full primitive equations employed in an OGCM. Moreover, their model forcing had 1-

135 day resolution and may have suppressed higher-frequency variability. Indeed, theoretical

136 analysis of internal wave generation by surface forcing [*Gill*, 1984], a recent numerical

₁₃₇ large eddy simulation [*Polton et al.*, 2008], and observations [*D'Asaro et al.*, 1995; *Alford*

₁₃₈ *and Whitmont*, 2007] all have shown that near-inertial processes are important in the

₁₃₉ ocean.

1.3. Estimates from in-situ data in this study

₁₄₀ In this study, we show how to isolate and estimate the wind energy input in the Ekman

₁₄₁ layer from in-situ data. This approach merits attention, if only because the concept of

₁₄₂ wind energy input to the Ekman layer has led to several estimates previously mentioned

₁₄₃ [*Wang and Huang*, 2004; *Huang et al.*, 2006] but none from in-situ observations of oceanic

₁₄₄ velocities on large scales. At least locally in the Southern Ocean, it complements other

₁₄₅ data-based estimates of the wind work on geostrophic motions. We here focus on the

₁₄₆ Southern Ocean (rather than the global ocean), because as previous studies have noted,

₁₄₇ it is the primary region for wind forcing to drive the ocean, and this wind energy is there-

₁₄₈ fore thought to contribute to wind-induced mixing needed to sustain the thermohaline

₁₄₉ structure of the world ocean [*Wunsch and Ferrari*, 2004].

₁₅₀ The steps leading to the development of the equations in this paper, their interpretation

₁₅₁ and the subsequent estimates were motivated by observations of coherent sub-inertial

₁₅₂ motions in drifter data [*Weller*, 1981; *McNally et al.*, 1989; *Niiler and Paduan*, 1995; *Rio*

₁₅₃ *and Hernandez*, 2003; *Elipot*, 2006]. This correlation as a function of frequency has been

₁₅₄ explained quite clearly by the development of Ekman theory extensions [*Gonella*, 1972;

₁₅₅ *Rudnick and Weller*, 1993; *Elipot and Gille*, 2008]. In this paper we derive a spectral

₁₅₆ energy equation and show that the wind energy input to the Ekman layer (i.e. the energy

₁₅₇ input in the oceanic boundary layer as represented by "Ekman" models) is equal to the

₁₅₈ real part of the cross-spectrum between the ocean surface velocity and the atmospheric

159 wind stress (section 2). First the cross-spectrum at the surface from surface drifter data

160 and reanalysis wind stress (section 3) is estimated; however, because drifter velocities

161 are not exactly representative of currents at the surface but at 15 m, some knowledge

162 of the vertical structure of the transfer function is needed to obtain the cross-spectrum

163 at the surface. The results from *Elipot and Gille* [2008] are used to infer the cross-

164 spectrum at the surface and therefore to estimate the wind energy input to the Ekman

165 layer zonally-averaged in the Southern Ocean (section 4). The results are discussed in

166 terms of spectral decomposition as well as latitudinal and seasonal variations. Section 5

167 provides a summary.

2. Spectral energy equation

168 The cross-spectrum between wind stress and ocean surface velocity serves as the pri-

169 mary diagnostic tool for this paper. It can be obtained theoretically from the horizontal

170 momentum balance. The derivation of a spectral energy equation shows that the real part

171 of the cross-spectrum, the co-spectrum, gives an estimate of the wind energy input rate

172 to the Ekman layer.

2.1. Spectral energy equation: the balance of spectra

173 The linearized horizontal momentum balance for the ocean in the absence of horizontal

174 pressure gradients is:

$$\frac{\partial \mathbf{u}(t,z)}{\partial t} + if\mathbf{u}(t,z) = \frac{1}{\rho}\frac{\partial \boldsymbol{\tau}(t,z)}{\partial z}, \tag{2}$$

176 where here $\mathbf{u}$ is the horizontal velocity, z the depth negative downward, $\boldsymbol{\tau}$ is the turbulent

177 Reynolds stress. The finite Fourier transform $\int_0^{\mathcal{T}}(\cdot)\exp(-i2\pi\nu_k t)dt$ of Eq. (2) is:

$$i(2\pi\nu_k + f)\mathbf{U}_k(\nu,z) = \frac{1}{\rho}\frac{\partial \mathbf{T}_k(\nu_k,z)}{\partial z}, \tag{3}$$

179 where $\mathbf{T}_k$ is the Fourier transform of $\boldsymbol{\tau}$. Multiplying Eq. (3) by $\mathbf{U}_k{}^*$ and integrating from

180 $z < 0$ to the surface $z = 0$ gives:

$$i\rho(2\pi\nu_k + f) \int_z^0 |\mathbf{U}_k|^2 \, dz = \int_z^0 \frac{\partial \mathbf{T}_k}{\partial z} \mathbf{U}_k{}^* dz. \tag{4}$$

182 Integrating by parts the right hand side yields:

$$i\rho(2\pi\nu_k + f) \int_z^0 |\mathbf{U}_k|^2 \, dz = \mathbf{T}_k \mathbf{U}_k{}^* \Big|_{z=0} - \mathbf{T}_k \mathbf{U}_k{}^* \Big|_z - \int_z^0 \mathbf{T}_k \left(\frac{\partial \mathbf{U}_k}{\partial z}\right)^* dz. \tag{5}$$

184 The first term on the right-hand side of Eq. (5) corresponds to the wind stress boundary

185 condition at the surface. The second term vanishes when we let z go to $-\infty$ to represent

186 the base of the wind-driven layer where velocities and/or turbulent stresses vanish, and

187 hence their Fourier transforms go to zero. Next, we apply to this equation the expected

188 value operator and divide by the length of the observation $\mathcal{T}$ to form a spectral energy

189 equation:

$$i(2\pi\nu_k + f)E + D = S_{\boldsymbol{\tau}\mathbf{u}}, \tag{6}$$

191 where

$$E = \rho \int_{-\infty}^0 \frac{\langle |\mathbf{U}_k|^2 \rangle}{\mathcal{T}} dz, \tag{7}$$

$$D = \int_{-\infty}^0 \frac{\left\langle \mathbf{T}_k \left(\frac{\partial \mathbf{U}_k}{\partial z}\right)^* \right\rangle}{\mathcal{T}} dz, \text{ and} \tag{8}$$

$$S_{\boldsymbol{\tau}\mathbf{u}} = \frac{\left\langle \mathbf{T}_k \mathbf{U}_k{}^* \Big|_{z=0} \right\rangle}{\mathcal{T}} \tag{9}$$

192 are estimates of the vertically integrated kinetic power spectral density of the Ekman

193 layer, the vertically integrated dissipated power spectral density in the Ekman layer, and

194 the power cross-spectrum between the wind stress and the ocean surface velocity. This

195 equation does not give the rate of change of energy but rather the average balance among

196 various power spectral quantities.

Next, we assume that the turbulent stress $\boldsymbol{\tau}$ is proportional to the vertical shear (following a classical diffusion model),

$$\frac{\boldsymbol{\tau}(t,z)}{\rho} = K(z)\frac{\partial \mathbf{u}(t,z)}{\partial z}. \tag{10}$$

The stress is aligned with the velocity vertical shear, implying that the vertical eddy viscosity K is real and independent of time. No additional assumptions are applied to K. The finite Fourier transform of Eq. (10) is:

$$\frac{\mathbf{T}_k}{\rho} = K\frac{\partial \mathbf{U}_k}{\partial z}. \tag{11}$$

Substituting (11) into (8) gives

$$D = \int_{-\infty}^{0} \rho K \frac{\left|\frac{\partial \mathbf{U}_k}{\partial z}\right|^2}{\mathcal{T}} dz \tag{12}$$

which is a real and positive quantity. The power cross-spectrum can be decomposed classically into real and imaginary parts:

$$S_{\boldsymbol{\tau}\mathbf{u}} = C_{\boldsymbol{\tau}\mathbf{u}} - i\,Q_{\boldsymbol{\tau}\mathbf{u}}, \tag{13}$$

where $C_{\boldsymbol{\tau}\mathbf{u}}$ is the coincident spectrum (co-spectrum) and $Q_{\boldsymbol{\tau}\mathbf{u}}$ is the quadrature spectrum (quad-spectrum). Thus, Eq. (6) splits into two equations:

$$D = C_{\boldsymbol{\tau}\mathbf{u}}, \tag{14}$$

$$-(2\pi\nu + f)E = Q_{\boldsymbol{\tau}\mathbf{u}}. \tag{15}$$

Eq. (14) describes the throughput of energy in each frequency band: the dissipated energy in the Ekman layer (i.e. the energy sink) equals the energy source given by the co-spectrum of the Ekman velocity at the surface and the wind stress. Eq. (15) states that the kinetic energy of the Ekman layer can be obtained from the quad-spectrum.

215 These equations resemble the spectral equations for atmospheric motions derived in the

216 time domain by *Chiu* [1970], who found that the spectral density of the kinetic energy is

217 shaped by quadrature spectral quantities and that the Coriolis parameter plays a role, as

218 is apparent in Eq. (15).

2.2. Total energy input rate to the Ekman layer

219   The Wiener-Khinchine theorem states that the frequency integral of the cross-spectrum

220 is equal to the complex cross-correlation function at zero time lag $\mathbf{R}_{\boldsymbol{\tau}\mathbf{u}}(0)$ [e.g. *Bendat*

221 *and Piersol*, 1986]:

$$\int_{-\infty}^{+\infty} S_{\boldsymbol{\tau}\mathbf{u}}(\nu)\,d\nu \;=\; \mathbf{R}_{\boldsymbol{\tau}\mathbf{u}}(0) \tag{16}$$

$$= \langle(\boldsymbol{\tau} - \langle\boldsymbol{\tau}\rangle)(\mathbf{u} - \langle\mathbf{u}\rangle)^*\rangle + \langle\boldsymbol{\tau}\rangle\langle\mathbf{u}^*\rangle. \tag{17}$$

222 For the real part this gives:

$$\int_{-\infty}^{+\infty} C_{\boldsymbol{\tau}\mathbf{u}}(\nu)\,d\nu = \mathcal{R}\left[\langle(\boldsymbol{\tau} - \langle\boldsymbol{\tau}\rangle)(\mathbf{u} - \langle\mathbf{u}\rangle)^*\rangle\right] + \mathcal{R}\left[\langle\boldsymbol{\tau}\rangle\langle\mathbf{u}^*\rangle\right], \tag{18}$$

224 which states mathematically that the integrated co-spectrum equals the real part of the

225 complex covariance of $\boldsymbol{\tau}$ and $\mathbf{u}$ plus the product of their time means. This does not imply

226 that the co-spectrum is the frequency distribution of the total work done on the ocean

227 by the wind stress. The spectral analysis of the latter quantity would include the work

228 on geostrophic currents and other processes including nonlinear forcings and interactions

229 between frequencies.

3. On obtaining the surface cross-spectrum from drifter data

3.1. Data

230   Ideally, the cross-spectrum discussed in the previous section would be computed using

231 time series of wind-driven velocity at the surface and contemporaneous wind stress time

232 series, at fixed locations, on a regular grid over the world ocean. However, observations

233 from moorings are too sparse to provide representative estimates on global scales, and their

234 shallowest velocity measurement depths are usually too far from the surface. Instead, here

235 we take advantage of velocity data derived from surface drifter trajectories. Drifter data

236 are not ideal to obtain the cross-spectrum at the surface and our estimates suffer from

237 non-negligeable uncertainties as well as some biases (see below). Nonetheless, we show

238 here that a first estimate from data of the wind energy input to the Ekman layer in this

239 region can be obtained and used as a benchmark for other indirect estimates. Such an

240 estimate may eventually be refined as our understanding of Southern Ocean boundary

241 layer dynamics improves.

242 To estimate the cross-spectrum, we use 40-day time series of wind stresses and

243 ageostrophic velocities. The latter were computed by subtracting surface geostrophic

244 velocities (see below) from drifter velocities. Drifter motions represent the currents aver-

245 aged over the 6.1 m length of a drogue, centered at 15 m depth. Therefore we interpret

246 the drifter velocities to be representative of oceanic velocities at 15-m depth, disregarding

247 the vertical shear over the length of the drogue [*Niiler et al.*, 1995].

248 Geostrophic velocities were derived from gradients of 7-day altimetric sea surface height

249 anomalies [AVISO], to which we added a time-mean geostrophic velocity computed from

250 GRACE satellite-derived dynamic topography [*Tapley et al.*, 2005]. Here we find that

251 the correlation between AVISO data and ECMWF data is not significant (not shown)

252 when these two datasets are interpolated along drifter trajectories. [In contrast, *Hughes*

253 *and Wilson* [2008] showed statistically significant correlation between wind stress and

254 altimeter-derived geostrophic velocities in the regions of the ocean comprising continental

slopes, the Equatorial region and extensions of western boundary currents.] Although the

AVISO/ECMWF correlation is not significant, the geostrophic component still must be

removed from the drifter velocity before computing the cross-spectrum. This is because

the integrated co-spectrum has a component arising from the time-mean components of

the drifter velocity and the wind stress velocity (second term on the left-hand side of

Eq. 17) that we would like to estimate as accurately as possible. Geostrophic compo-

nents left in the mean or anomaly fields could lead to an erroneous estimate of the mean

ageostrophic velocity.

For wind data, we use European Center for Medium-Range Weather Forecasts

(ECMWF) ERA-40 Project re-analysis wind stresses [*Simmons and Gibson*, 2000] ob-

tained from the Data Support Section of the Scientific Computing Division at the National

Center for Atmospheric Research. ECMWF wind stresses are released on a Gaussian grid

with resolution of 1.125° longitude by roughly 1.125° latitude at 6 hour sampling. These

grids were linearly interpolated on the drifter positions to obtain contemporaneous time

series of wind stress. Using drifter velocity time series without taking into account their

Lagrangian nature is equivalent to assuming horizontal homogeneity when writing the

momentum equation (2). This assumption is justified by the fact that the spatial length

scales of the local wind stress events driving Ekman or inertial currents are larger than the

length scales of the drifter motions. As in *Elipot and Gille* [2008], spectral estimates by

the periodogram method and formal errors were computed following *Bendat and Piersol*

[1986]. See *Elipot and Gille* [2008] for more details.

3.2. The shear bias

276   Drifter velocities are interpreted as 15 m velocities so that the cross-spectrum with the

277 wind stress is not the quantity that we seek to estimate (Eq. 9) and a correction for

278 this shear bias needs to be implemented. At subinertial frequencies, a model with vertical

279 shear for wind-driven velocity is preferable to a slab model [e.g. *Weller and Plueddemann*,

280 1996; *Elipot and Gille*, 2008]. In the spectral domain, the transfer function theoretically

281 links the auto-spectrum of the wind stress to the cross-spectrum of the wind stress and

282 the velocity at depth z [*Elipot and Gille*, 2008]:

$$S_{\boldsymbol{\tau}\mathbf{u}}(\nu, z) = \mathbf{H}(\nu, z)S_{\boldsymbol{\tau}\boldsymbol{\tau}}(\nu). \tag{19}$$

284 The real part of (19) is:

$$C_{\boldsymbol{\tau}\mathbf{u}}(\nu, z) = \mathcal{R}\left[\mathbf{H}(\nu, z)\right] S_{\boldsymbol{\tau}\boldsymbol{\tau}}(\nu) \tag{20}$$

286 Applying this expression for $z = 0$ and $z = -15$, the depth of a drifter's drogue, the

287 co-spectrum of the wind stress and the ocean velocity is:

$$
\begin{aligned}
C_{\boldsymbol{\tau}\mathbf{u}}(\nu, 0) &= \frac{\mathcal{R}\left[\mathbf{H}(\nu, 0)\right]}{\mathcal{R}\left[\mathbf{H}(\nu, -15)\right]}C_{\boldsymbol{\tau}\mathbf{u}}(\nu, -15) \tag{21} \\
&= R \times C_{\boldsymbol{\tau}\mathbf{u}}(\nu, -15). \tag{22}
\end{aligned}
$$

288 R is a shear correction coefficient that can be derived from the transfer function $\mathbf{H}$. *Elipot*

289 *and Gille* [2008] estimated the transfer function from the same drifter and wind stress

290 data used in this study. They fitted these observed transfer functions to analytic transfer

291 function that used different expressions for the oceanic boundary layer and for vertical

292 viscosity and then sought best estimates of viscosity and boundary layer parameters in

293 order to minimize misfit between observations and theory. They found that the overall

294 best model across the Southern Ocean is a 1-layer model with a constant viscosity O(0.01-

295 0.1) m^2 s^{-1} and a boundary layer depth O(30-50) m, with latitudinal variations. Here

296 we use the parameters from this model to compute R to obtain the co-spectrum at the

297 surface by Eq. 21.

298   Theoretically, $1/R$ is less than one and more convenient to plot. Fig. 1 shows $1/R$ as a

299 function of latitude and frequency from the results of *Elipot and Gille* [2008].

3.3. The slip bias

300   Surface drifters are slightly imperfect water-followers, and their measurements include

301 an erroneous slip velocity thought to be caused by two phenomena: First, the direct action

302 of the wind on the surface flotation buoy, and second the vertical shear of the horizontal

303 velocity across the vertical extend of the drogue. *Niiler et al.* [1995] estimated the slip $\mathbf{u}_s$

304 using vector measuring current meters mounted on the top and bottom of the drogues for

305 a select group of drifters released in the tropical and northeastern Pacific. They modeled

306 the slip as:

$$\mathbf{u}_s = \frac{a}{A}\mathbf{w}_{10} + \frac{b}{A}\Delta\mathbf{u}, \tag{23}$$

308 where $\mathbf{w}_{10}$ is the 10-m wind velocity, A is the drag area ratio of the drogue to the other

309 constituents of a drifter (40 for a SVP-type drifter) and $\Delta\mathbf{u}$ is the velocity difference

310 measured between the top and bottom of the drogue. Since $\Delta\mathbf{u}$ cannot be determined

311 from drifter data alone, here we do not attempt to evaluate the second term in (23).

312 We correct drifter velocities for wind slip using $a = 4.63 \times 10^{-2}$ [*Niiler et al.*, 1995]

313 and determining $\mathbf{w}_{10}$ from ECMWF 10-m winds interpolated in space and time to drifter

314 locations. As noted by [*Niiler et al.*, 2003], the wind slip correction may be underestimated

315 in the Southern Ocean, where mean wind speeds often exceed 10 m s^{-1}, the upper limit

316 for which estimates of a have been validated.

³¹⁷   The basic impact of this slip correction is to modify the estimates of the cross-spectrum,

³¹⁸   but it potentially acts at two steps of the wind energy input computation. First, *Elipot and*

³¹⁹   *Gille* [2008] found that applying the wind slip correction tends to increase the magnitude of

³²⁰   the vertical viscosity and of the boundary layer depth. This in turn reduces the shear from

³²¹   the surface to 15 m depth. Second, the wind slip correction also reduces the magnitude

³²²   of the co-spectrum and increases the quad-spectrum. Correspondingly, this reduces the

³²³   inferred co-spectrum of the wind stress and the surface ocean velocity after applying

³²⁴   the shear correction. Finally, the estimates for the energy input rate D are accordingly

³²⁵   reduced. North of 54° S, the reduction averages 32%, but it is only 13% south of this

³²⁶   latitude, equivalent to a 3 and 17×10^{-3} W m^{-2} reduction across the Southern Ocean,

³²⁷   with an average decrease of 8.6×10^{-3} W m^{-2}. These uncertainties could seem deceptively

³²⁸   large but are in fact reasonable for a first estimate of this type of wind energy input from

³²⁹   in-situ data. It also clearly calls for further research into the dynamics of the boundary

³³⁰   layer as well as the behavior of SVP drifters in high wind environments.

4. Results and Discussion

³³¹   To summarize the method, we compute the co-spectrum at 15 m, estimate the surface

³³²   co-spectrum following Eq. 21, and then sum the surface co-spectrum over the frequency

³³³   range resolved in this study (from -2 cpd to 2 cpd) to obtain the wind energy input

³³⁴   following the left-hand side of Eq. 18. At this stage the reader may wonder why we do

³³⁵   not simply compute the cross-covariance between $\boldsymbol{\tau}$ and $\mathbf{u}$, that is the right-hand side of

³³⁶   Eq. 18? The first reason is that the shear correction depends on the frequency of the

³³⁷   motions (as shown clearly by Fig. 1) and cannot be applied to only the cross-covariance, as

³³⁸   pointed out by *Crawford and Large* [1996]. Second, by retaining the frequency information

339 we gain a useful diagnostic of the frequencies that matter for the process under scrutiny,

340 as will be shown in section 44.3.

341   In order to study latitudinal and seasonal variability, the total drifter dataset is divided

342 in 2° latitudinal bands, without regard for dynamical regime. Co-spectra were estimated

343 in each of these bands and integrated over specified frequency ranges. Figure 3 shows

344 results for the year-round dataset, and Fig. 4 shows results for austral winter (blue) and

345 summer (red).

4.1. Year-round data

346   The total energy input rate is plotted in black in Fig. 3a. It differs by more than a factor

347 of 5 across the Southern Ocean, ranging from a minimum of $(9.8 \pm 0.3) \times 10^{-3}$ W m^{-2}

348 at 31° S to a maximum of $(53 \pm 3) \times 10^{-3}$ W m^{-2} at 57° S. We split the total energy

349 into contributions from the mean, or zero frequency, (light gray line) and contributions

350 from the time-varying components (dark gray line). Both increase from north to south,

351 the mean by more than a factor of 10 and the time-varying contribution by a factor of

352 4. Fig. 3b shows that their relative contributions are comparatively consistent at all

353 latitudes, with the mean having its most significant impact at 51° S, where it accounts

354 for 28% of wind energy input. Wind stress, shown in Fig. 3c is largest at 53° S for the

355 mean (light gray), the variance (dark gray), and the total (black).

356   Fig. 3d shows the energy input rate to the Ekman layer split into cyclonic and anticy-

357 clonic frequencies. It is predominantly anticyclonic at almost all latitudes in the Southern

358 Ocean, except southward of 57° S where about an equal amount of energy is input through

359 cyclonic and anticyclonic frequencies. The relative contributions of the anticyclonic and

360 cyclonic frequencies are plotted in Fig. 3e: the anticyclonic contribution decreases from

361 72% at 31° S to 50% at 59° S. (For this plot, the contribution of the mean is partitioned

362 equally between the two frequency domains.) This anticyclonic predominance is a conse-

363 quence of two factors. First, as shown in Fig. 3f, the mean-squared wind stress forcing is

364 larger for anticyclonic frequencies (dashed lines) than for cyclonic frequencies (solid lines)

365 across the Southern Ocean. [The mean-squared wind stress $\langle \tau^2 \rangle$ is about 70% anticyclonic

366 frequencies at 31° S, decreasing to about 53% anticyclonic at 59° S (not shown).] Second,

367 if the oceanic response were flat, then the ocean currents would exactly reflect the par-

368 titioning of the wind. Instead, here the ocean response is more strongly anticylonic, due

369 to the preferential anticylonic response of the ocean, as predicted by theoretical Ekman

370 models [*Elipot and Gille*, 2008].

371   The third row of Fig. 3 shows the impact of near-inertial frequencies taken from $\nu =$

372 $-f/2\pi/2$ to 2 cpd. In Fig. 3g, the energy input rate in near-inertial frequency range

373 (gray line, here multiplied by 10 for legibility) increases with latitude, peaks at 45° S

374 and decreases further south. Similarly, in Fig. 3i, the variance of the near-inertial wind

375 stress (gray, again multiplied by 10 for legibility) increases from 31° S to 45° S, then stays

376 almost constant to 53° S, and finally decreases towards 59° S. The relative importance of

377 the near-inertial to non-inertial frequencies (Fig. 3h) is quite modest, always less than

378 7%. The contribution from the near-inertial band is somewhat surprising. Why does

379 the contribution from the near-inertial frequencies peak at latitudes to the north of the

380 contribution from all the non-zero frequencies? There may be two reasons for this drop

381 in the co-spectrum: first the low variance in ECMWF wind stress at higher latitudes

382 [*Gille*, 2005], and second the drop of variance in the inertial band for drifter data towards

383 higher latitudes because of the 12-hour interval used for computing drifter velocities which

approaches the local inertial frequency [*Lumpkin and Pazos*, 2007; *Elipot and Lumpkin*, 2008]. The existence of strong inertial oscillations in the Southern Ocean has recently been shown in the drifter data [*Chaigneau et al.*, 2008] that have not been regridded in time using the kriging procedure described in *Lumpkin and Pazos* [2007]. Thus the contribution from near-inertial frequencies is likely underestimated with the datasets used for this study.

4.2. Seasonal variability

The wind energy input rate estimates were recomputed after sorting the data between a summer season and a winter season. In general, the seasonal variability manifests itself latitudinally and also as a function of the frequency range considered.

From summer to winter, south of 48° S, the energy input rates from the mean (light blue and light red lines in Fig.4a) are not distinguishable within the error bars. North of this latitude the differences are statistically significant. The energy input rates from the non-zero frequencies (medium blue and medium red lines) increase by 69% on average from summer to winter. This increase also varies latitudinally, roughly decreasing from north to south, with almost twice the fractional seasonal difference at 39° S than at 55° S. As a consequence, since the total energy input (dark red and blue lines in Fig. 4a) is dominated by the non-zero frequencies, from summer to winter, the total input is increased on average by 67%, but this seasonal increase varies greatly: south of 42° S it averages to 42%, but north of 42° S it averages to 105%.

Although total energy input changes seasonally, the partitioning between anticylonic and cyclonic components does not. Figs. 4d, e and f indicate no qualitative differences as a function of seasons.

The wind energy input in the near-inertial range (Fig. 4g) does show an increase from summer to winter, between 5% and 122% across the Southern Ocean. This pattern follows the trend of increased wind stress variance in winter in the near-inertial band, but it is less dramatic since the near-inertial variance of the wind stress can be multiplied by a factor up to 2.5.

4.3. Frequency decomposition of the input

For the purpose of discussing further the frequency decomposition of the energy input and comparing to previous estimates of the wind energy input, Fig. 2 shows the cumulative integration from $|\nu| = 0$ to 2 cpd of the surface co-spectrum from data in the zonal band centered around 41° S for anticyclonic frequencies (dashed curves), cyclonic frequencies (thin solid curve) and both frequencies (heavy solid curve). The results in all other latitudinal bands are fairly similar to what is observed at 41° S.

Anticyclonic frequencies (dashed lines) contribute more to the total energy input than the cyclonic frequencies (thin solid lines), and this is true for all frequency ranges greater than zero. Again, this is due to a greater anticyclonic wind stress forcing reinforced by a greater anticyclonic response [*Elipot and Gille*, 2008]. This is a potential explanation for the predominance of anticyclonic "spin" in the Southern Ocean at these latitudes as revealed by the study of *Griffa et al.* [2008].

Time-varying components dominate the energy input relative to the zero-frequency contribution, as is also evident for all latitudes of the Southern Ocean in Fig. 3a. Motions at frequencies higher than $(20)^{-1}$ cpd actually generally contibute to more than about 50% of the total. This is in contrast with the time scales at which potential energy is thought to increase via the work on geostrophic motions: *Wunsch* [1998] found in his estimate of

Eq. (1) that the contribution from the time mean accounted for about 94% of the global

average value. However, the time-varying components were resolved up to approximately

$(20)^{-1}$ cpd only, the Nyquist frequency for T/P orbit repeat period, and contributions

from higher frequencies, especially arising from wind fluctuations, were believed to be

very small. *Hughes and Wilson* [2008] recomputed the wind energy input into geostrophic

motions using updated altimetry data and scatterometer data, and their global integrals

imply that the contribution of the time mean exceeds in fact 98% of the total.

Wang and Huang's (2004) estimates of the wind energy input to the Ekman layer, which

varied approximately between 12 and 20 $\times$ 10 $^{-3}$ W m^{-2} in the ACC region (see their

Fig. 3), included only the contribution from frequencies up to $|\nu| = 1/2$ cpd. For our

estimates the contribution from this same frequency range (with an upper limit indicated

by a vertical gray line in Fig. 2) are generally larger, here $20.8 \pm 0.5 \times 10^{-3}$ W m^{-2} at

41° S in Fig. 2 but maximum with $49 \pm 3 \times 10^{-3}$ W m^{-2} at 57° S (not shown). For their

estimates, *Wang and Huang* used a theoretical model to compute the Ekman velocities

at the surface. Their model assumes an infinitely deep ocean and a constant vertical

viscosity. *Elipot and Gille* [2008] found this model to be the worst of 9 simple models

that they tested. For the purpose of the wind energy input, the *Wang and Huang* model

underestimates the co-spectrum because it requires that the velocities at the surface be

directed 45° from the wind stress direction and therefore underestimate the energy input.

Moreover, we find that higher frequencies from $|\nu| = 0.525$ to 2 cpd, neglected by *Wang*

and Huang [2004], add a non-negligeable contribution, here about $2.6 \pm 0.8 \times 10^{-3}$ W m^{-2}

at 41° S or 11% of the total. Overall, the high-frequency contribution varies between 7%

and 12% for the latitudes considered here. As mentioned previously, the variance of the

wind stress from numerical weather reanalyses as well as drifter data may be too low

at high latitudes, and consequently the contribution from these frequencies may even be

underestimated.

In the "near-inertial" frequency range, from $\nu = -f/2\pi/2$ to 2 cpd, the anticyclonic

frequencies input $1.40 \pm 0.02 \times 10^{-3}$ W m^{-2} at 41° S, 6% of the total. Over the Southern

Ocean as a whole, this percentage varies from 1.5% to 7% and is typically the same

order of magnitude as the energy flux into wind-forced near-inertial mixed-layer motions

over broad oceanic regions, as estimated from a slab-layer model [e.g. *Alford*, 2001]. These

numbers imply that at least for the Southern Ocean, the wind energy is input to the Ekman

layer predominantly at subinertial frequencies and not in the inertial band. However, the

contribution of the near-inertial frequency range is likely underestimated in these datasets.

Elipot and Lumpkin [2008] showed that much more energy is present in this band when the

raw-drifter dataset is used compared to the historical 6-hourly kriged dataset. A definite

answer to this uncertainty in the contribution of high frequencies at high latitude for the

energy input rate in the Ekman layer is not likely to be accessible until higher temporal

wind information (that is higher frequency sampling than 6 hours) is available.

5. Summary

A classic diffusion model, in which the turbulent stress is proportional to the vertical

shear of the horizontal velocity, is used in the horizontal momentum balance equation of

the ocean in the absence of large-scale pressure gradient in order to derive a spectral energy

equation. In this framework, the real part of the cross-spectrum between the atmospheric

stress upon the ocean and the surface ocean velocity is a measure as a function of frequency

of the energy input "to the Ekman layer". This energy is dissipated throughout the depth

⁴⁷³ of the oceanic boundary layer and may be passed below and is an important potential

⁴⁷⁴ contributor to the mechanical energy budget of the ocean.

⁴⁷⁵ Surface drifter data, altimeter data, and reanalysis wind stresses are used to estimate

⁴⁷⁶ first the zonally-averaged cross-spectrum between the wind stress and 15-m ageostrophic

⁴⁷⁷ velocities for absolute frequencies of motions between 0 and 2 cpd, in the Southern Ocean.

⁴⁷⁸ Because drifter velocities are not exactly representative of currents at the surface but at

⁴⁷⁹ 15 m, some knowledge of the vertical structure of the transfer function is needed to obtain

⁴⁸⁰ the cross-spectrum at the surface. The results from *Elipot and Gille* [2008] are used to

⁴⁸¹ infer the cross-spectrum at the surface and therefore to estimate the wind energy input

⁴⁸² to the Ekman layer in this region.

⁴⁸³ The spectral characteristics of this energy input are studied, notably its polarization.

⁴⁸⁴ Results show that the combination of a stronger anticyclonic wind stress forcing associ-

⁴⁸⁵ ated with a greater anticyclonic response makes the contribution from the anticyclonic

⁴⁸⁶ frequencies dominate the wind energy input, providing a potential explanation for the

⁴⁸⁷ predominance of anticyclonic motions at these latitudes.

⁴⁸⁸ The latitudinal and seasonal variations of the wind energy input to the Ekman layer are

⁴⁸⁹ closely related to the variations of the wind stress, for the mean and for the time-varying

⁴⁹⁰ components. From these, the contribution from the near-inertial band follows a different

⁴⁹¹ trend, increasing from low latitudes to only about 45° S to decrease further south, possibly

⁴⁹² a consequence of the lack of variance in the drifter and wind stress data.

⁴⁹³ The uncertainties arising from the drifter data could potentially modify our quantitative

⁴⁹⁴ results by up to 30%. However, we argue here that surface drifter velocities can be used

⁴⁹⁵ to obtain global estimates of the wind energy input, provided that we obtain a good

understanding of vertical viscosity and boundary layer depth so that the surface cross-spectrum can be obtained from the 15 m cross-spectrum. This is of potential great importance as high frequency forcing and variability of the ocean is related to the sources of kinetic energy and near-inertial waves that are related to the mixing of the ocean and the global overturning circulation.

References

Alford, M. H. (2001), Internal swell generation: The spatial distribution of energy flux from the wind to mixed layer near-inertial motions, *J. Phys. Oceanogr.*, *31*, 2359–2368.

Alford, M. H. (2003), Improved global maps and 54-year history of wind-work on ocean inertial motions, *Geophys. Res. Lett.*, *30*(8), 1424, doi:10.1029/2002GL016614,2003, 1424,10.1029/2002GL016614,2003.

Alford, M. H., and M. Whitmont (2007), Seasonal and Spatial Variability of Near-Inertial Kinetic Energy from Historical Moored Velocity Records, *J. Phys. Oceangr.*, *37*(8), 2022–2037.

AVISO (1996), *AVISO User Handbook for Merged TOPEX/POSEIDON products*, AVISO/Altimetry, Ramonville-Saint-Agne, France, AVI-NT-02-101-CN, 3.0 ed.

Bendat, J. S., and A. G. Piersol (1986), *Random data. Analysis and measurements pro-*

    cedures, Third Edition, John Wiley & Sons, 594 pp.

Chaigneau, A., O. Pizarro, and W. Rojas (2008), Global climatology of near-inertial

    current characteristics from Lagrangian observations, *Geophys. Res. Lett*, *35*, L13,603,

    doi:10.1029/2008GL034060.

Chiu, W.-C. (1970), On the spectral equations and the statistical energy spectrum of

    atmospheric motions in the frequency domain, *Tellus*, *22*(6), 608–619.

Crawford, G. B., and W. G. Large (1996), Numerical investigation of resonant inertial

    response of the ocean to wind forcing, *J. Phys. Oceanogr.*, *26*(6), 873–891.

D'Asaro, E. A. (1985a), The energy flux from the wind to near-inertial motions in the

    surface mixed layer, *J. Phys. Oceanogr.*, *15*(8), 1043–1059.

D'Asaro, E. A. (1985b), Upper ocean temperature structure, inertial currents, and

    Richardson numbers observed during strong meteorological forcing, *J. Phys. Oceanogr.*,

    15(7), 943–962.

D'Asaro, E. A., C. C. Eriksen, M. D. Levine, P. Niiler, C. A. Paulson, and P. Van Meurs

    (1995), Upper-ocean inertial currents forced by a strong storm. Part I: Data and com-

    parisons with linear theory, *J. Phys. Oceanogr.*, *25*(11), 2909–2936.

Duhaut, T. H. A., and D. N. Straub (2006), Wind Stress Dependence on Ocean Surface

    Velocity: Implications for Mechanical Energy Input to Ocean Circulation, *J. Phys.*

    Oceanogr., *36*(2), 202–211.

Ekman, V. W. (1905), On the influence of the Earth's rotation on ocean currents, *Ark.*

    Mat. Astr, Fys., *2*(11), 1–36.

538 Elipot, S. (2006), Spectral characterization of ekman velocities in the southern ocean

539   based on surface drifter trajectories, Ph.D. thesis, Scripps Institution of Oceanography,

540   University of California, San Diego.

541 Elipot, S., and S. Gille (2008), Ekman layers in the Southern Ocean: spectral models and

542   observations, vertical viscosity and boundary layer depth, submitted to the J. Mar. Res.

543 Elipot, S., and R. Lumpkin (2008), Spectral description of oceanic near-surface variability,

544   *Geophys. Res. Lett*, *35*, L05,606, doi:10.1029/2007GL032874.

545 Ferrari, R., and C. Wunsch (2008), Ocean circulation kinetic energy: Reservoirs, sources

546   and sinks, *Ann. Rev. Fluid Mech.*, in press.

547 Fofonoff, N. P. (1981), The Gulf Stream, in *Evolution of Physical Oceanography: scientific*

548   *surveys in honor of Henry Stommel*, edited by B. A. Warren and C. Wunsch, pp. 112–

549   139, MIT Press.

550 Gill, A. E. (1984), On the Behavior of Internal Waves in the Wakes of Storms, *J. Phys.*

551   *Oceanogr.*, *14*(7), 1129–1151.

552 Gill, A. E., J. S. A. Green, and A. Simmons (1974), Energy partition in the large-scale

553   ocean circulation and the production of mid-ocean eddies, *Deep-Sea Res.*, *21*, 499–528.

554 Gille, S. T. (2005), Statistical characterization of zonal and meridonal ocean wind stress,

555   *J. Atmos. Oceanic Technol.*, *22*(9), 1353–1372.

556 Gonella, J. (1972), A rotary-component method for analysing meteorological and oceano-

557   graphic vector time series, *Deep-Sea Res.*, *19*, 833–846.

558 Gregg, M. C. (1987), Diapycnal mixing in the thermocline: a review, *J. Geophys. Res.*,

559   *92*, 5249–5286.

560 Griffa, A.-L., R. Lumpkin, and M. Veneziani (2008), Cyclones and anticyclones in the

561   upper ocean: from large eddies to submesoscale, *Geophys. Res. Lett.*, *35*, L01,608, doi:

562   10.1029/2007GL032100.

563 Huang, R. X., W. Wei, and L. L. Liu (2006), Decadal variability of wind-energy input to

564   the world, *Deep-Sea Res. Pt II*, *53*(1-2), 31–41.

565 Hughes, C., and C. Wilson (2008), Wind work on the geostrophic ocean circulation: An

566   observational study of the effect of small scales in the wind stress, *J. Geophys. Res*, *113*,

567   doi:10.1029/2007JC004371.

568 Large, W. G., J. C. McWilliams, and S. C. Doney (1994), Oceanic vertical mixing: a review

569   and a model with a nonlocal boundary layer parameterization, *Reviews of Geophysics*,

570   *32*, 363–404, doi:10.1029/94RG01872.

571 Lumpkin, R., and M. Pazos (2007), Measuring surface currents with SVP drifters: the

572   instrument, its data, and some recent results, in *Lagrangian Analysis and Prediction of*

573   *Coastal and Ocean Dynamics*, edited by A. Griffa, A. D. Kirwan, A. Mariano, T. Oz-

574   gokmen, and T. Rossby, pp. 39–67, Cambridge University Press.

575 McNally, G. J., D. S. Luther, and W. B. White (1989), Subinertial frequency response of

576   wind-driven currents in the mixed layer measured by drifting buoys in the midlatitude

577   North Pacific, *J. Phys. Oceanogr.*, *19*, 290–300.

578 Niiler, P. P., and J. D. Paduan (1995), Wind-driven motions in the Northeast Pacific as

579   measured by Lagrangian drifters, *J. Phys. Oceanogr.*, *25*(11), 2819–2830.

580 Niiler, P. P., A. L. Sybrandy, K. Bi, P. Poulain, and D. Bitterman (1995), Measurements

581   of the water-following capability of holey-sock and TRISTAR drifters, *Deep-Sea Res.*,

582   *42*, 1951–1964.

583 Niiler, P. P., N. A. Maximenko, and J. C. McWilliams (2003), Dynamically bal-

584 anced absolute sea level of the global ocean derived from near-surface veloc-

585 ity observations, *Geophys. Res. Let.*, *30*(22), 2164, doi:doi:10.1029/2003GL018628,

586 doi:10.1029/2003GL018628.

587 Plueddemann, A. J., and J. T. Farrar (2006), Observations and models of the energy flux

588 from the wind to mixed-layer inertial currents, *Deep-Sea Res.*, *53*(1-2), 5–30.

589 Pollard, R. T., and R. C. J. Millard (1970), Comparison between observed and simulated

590 wind-generated inertial oscillations, *Deep-Sea Res.*, *17*, 813–821.

591 Polton, J. A., J. A. Smith, J. A. MacKinnon, and A. E. Tejada-Martínez (2008), Rapid

592 generation of high-frequency internal waves beneath a wind and wave forced oceanic

593 surface mixed layer, *Geophys. Res. Lett*, *35*, L13,602, doi:10.1029/2008GL033856.

594 Poulain, P.-M. (1990), Near-inertial and diurnal motions in the trajectories of mixed layer

595 drifters, *J. Mar. Res.*, *48*, 793–823.

596 Rio, M. H., and F. Hernandez (2003), High-frequency response of wind-driven currents

597 measured by drifting buoys and altimetry over the world ocean, *J. Geophys. Res.*,

598 *108*(C8), 3283, doi:10.1029/2002JC001655, doi: 10.1029/2002JC001655.

599 Rudnick, D. L., and R. A. Weller (1993), Observations of Superinertial and Near-Inertial

600 Wind-driven Flow, *J. Phys. Oceanogr.*, *23*(11), 2351–2359.

601 Simmons, A. J., and J. K. Gibson (2000), ERA-40 project report series n0.1: The ERA-40

602 project plan, *Tech. rep.*, European Center for Medium-range Weather Forecasts.

603 Stern, M. E. (1975), *Ocean Circulation Physics*, Academic Press, 275 pp.

604 Tapley, B., et al. (2005), GGM02 - An improved Earth gravity field model from GRACE,

605 *J. Geod.*, *79*(8), 467–478.

Von Storch, J. S., H. Sasaki, and J. Marotzke (2007), Wind-Generated Power Input to the

Deep Ocean: An Estimate Using a 1/10 General Circulation Model, *J. Phys. Oceanogr.*,

37(3), 657–672.

Wang, W., and R. Huang (2004), Wind energy input to the Ekman layer, *J. Phys.

Oceanogr, 34*(5), 1267–1275.

Watanabe, M., and T. Hibiya (2002), Global estimates of the wind-induced energy flux

to inertial motions in the surface mixed layer, *Geophys. Res. Lett., 29*(8), 1239, doi:

doi:10.1029/2001GL014422,2002, 1239,10.1029/2001GL014422,2002.

Weijer, W., and S. T. Gille (2005), Energetics of wind-driven barotropic variability in the

Southern Ocean, *J. Mar. Res., 63*(6), 1101–1125.

Weller, R. A. (1981), Observations of the velocity response to wind forcing in the upper

ocean, *J. Geophys. Res., 86*(C3), 1969–1977.

Weller, R. A., and A. J. Plueddemann (1996), Observations of the vertical structure of

the oceanic boundary layer, *J. Geophys. Res., 101*(C4), 8789–8806.

Wunsch, C. (1998), The work done by the wind on the oceanic general circulation, *J.

Phys. Oceanogr., 28*(11), 2332–2340.

Wunsch, C., and R. Ferrari (2004), Vertical mixing, energy, and the general circulation of

the oceans, *Ann. Rev. Fluid Mech., 36*(1), 281–314.
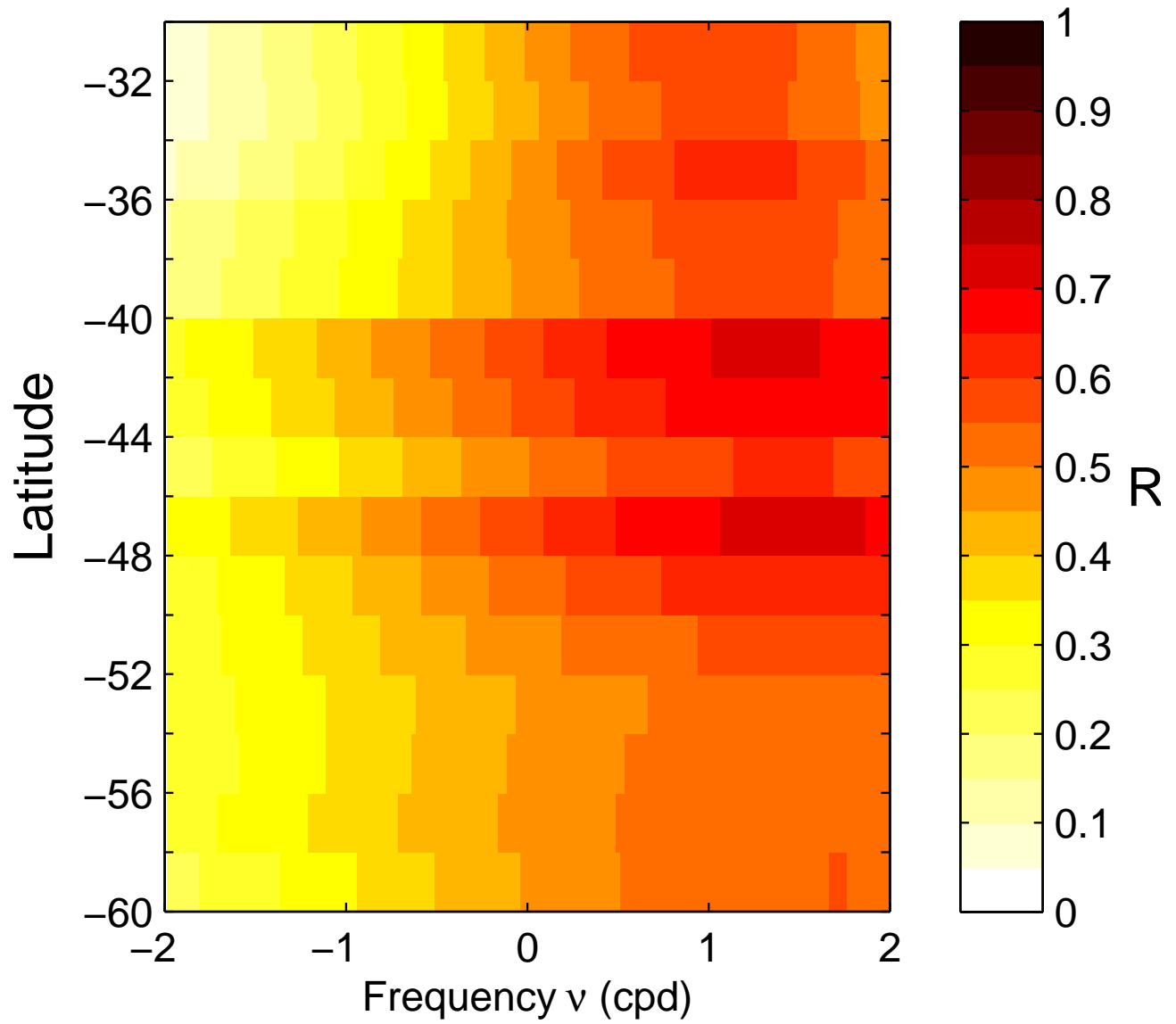
Figure 1. Ratio of the co-spectrum at 15 m to the co-spectrum at the surface.
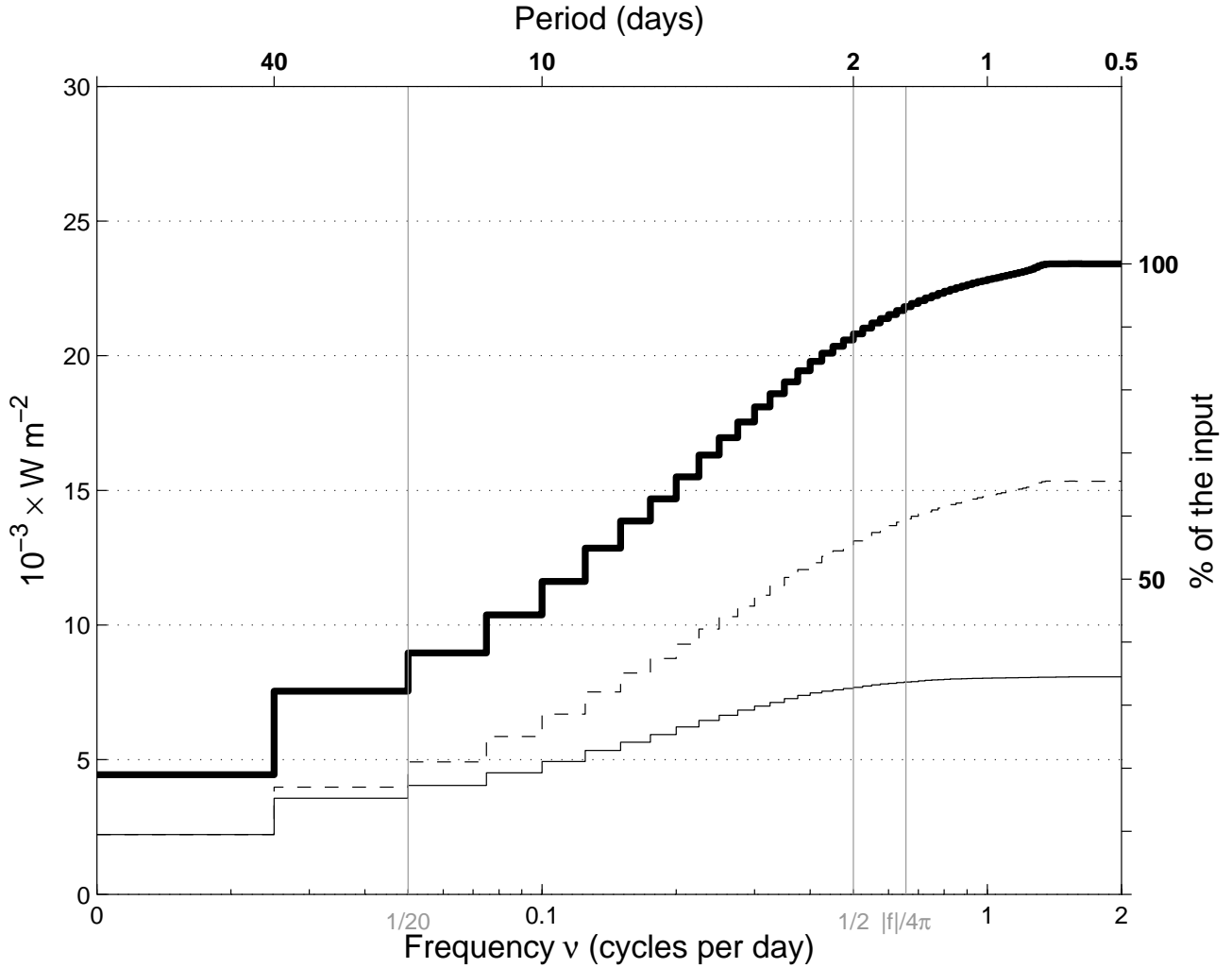
**Figure 2.**   Cumulative integration of the co-spectra at the surface at 41° S for anticyclonic frequencies (dashed curve), cyclonic frequencies (thin solid curve) and the sum of anticyclonic and cyclonic frequencies (solid heavy curve). The axis of the abscissas is on a logarithmic scale but the lowest frequency plotted in each case is the zero frequency contribution, which is split evenly between the anticyclonic and cyclonic domains. Vertical lines mark specific frequencies.
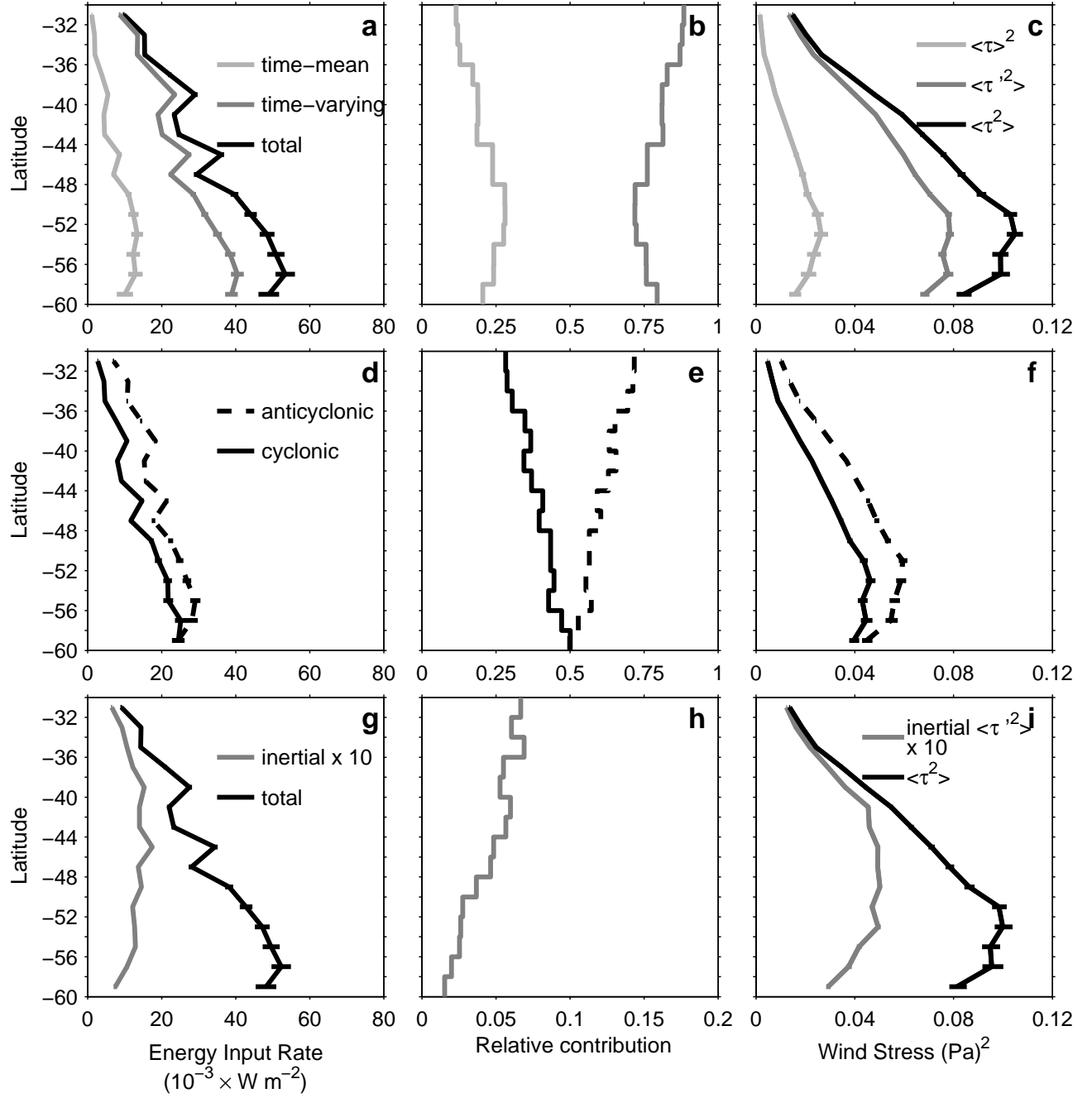
Figure 3.   Energy input rates across the Southern Ocean. (a) Contributions from the mean, the non zero frequencies and total within each latitudinal band. (b) Relative contributions of the zero frequency and of the non zero frequencies in the total energy input rate. (c) Mean value square, variance and mean square value of the wind stresses interpolated on the drifter positions. (d) Energy input rate contributions from the anticyclonic and the cyclonic frequencies. (e) Relative contribution of the anticyclonic and cyclonic frequencies for the total energy input rate. (f) Mean square value (variance plus half of the mean) of the wind stresses for anticyclonic and cyclonic frequencies. (g) Contribution from the near-inertial frequencies multiplied by 10 for legibility and contribution from the remaining frequencies. (h) Relative contribution of the near inertial frequencies for the total energy input rate. Note the change of scale for the abscissa compared to panels b and e. (i) Wind stress variance for the near-inertial frequencies multiplied by 10 for legibility and mean square value for the remaining frequencies. Error bars for the energy input rate are derived from the standard errors for the co-spectra. Error bars for the wind stress variance are derived from the formal 95% confidence intervals of the wind stress spectra.
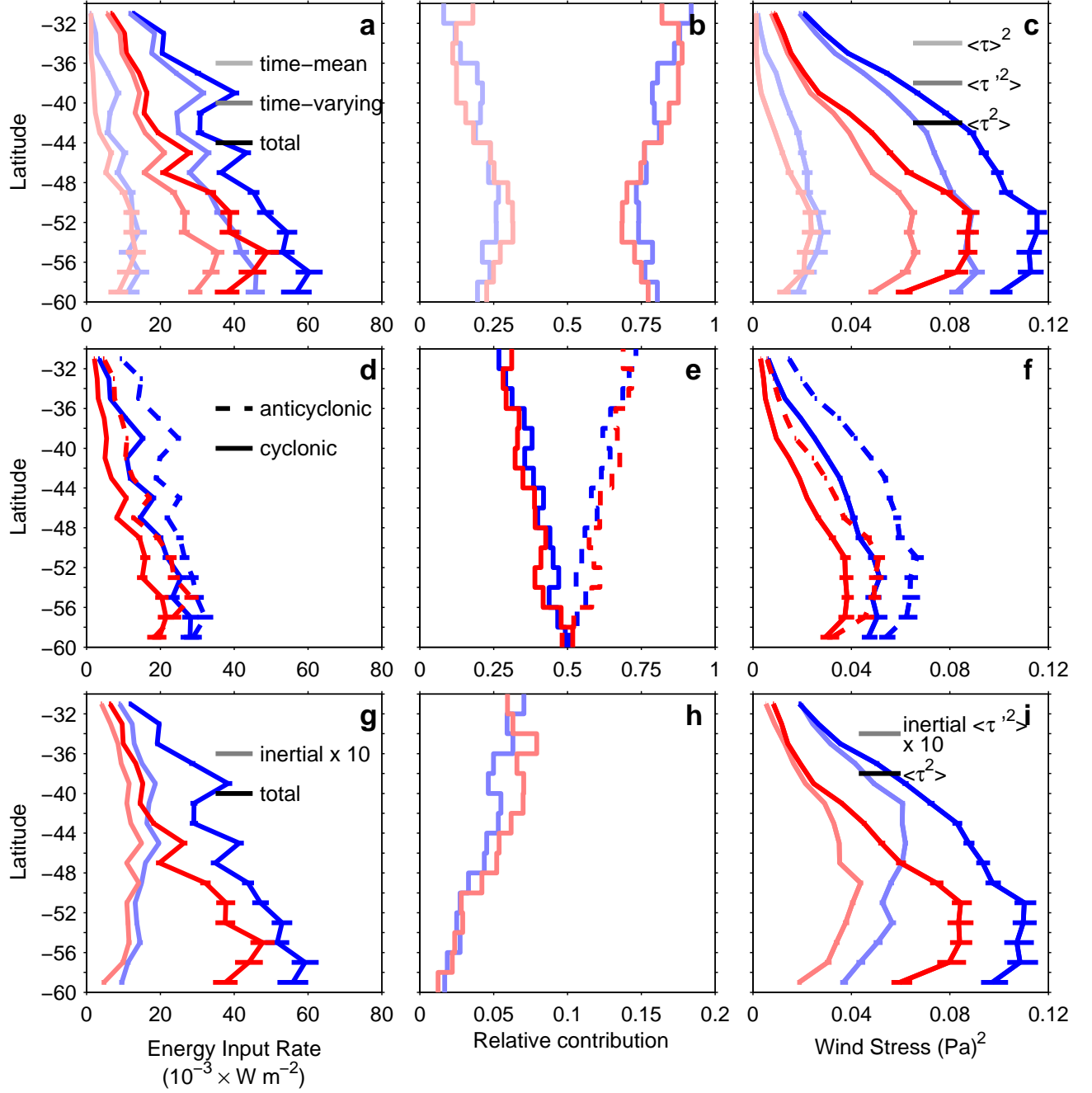
Figure 4. Energy input rates across the Southern Ocean as a function of season. Blue shading: austral winter, red shading: austral summer. For the description of each panel see the caption of Fig. 3.